J. Fluid Mech. (2022), *vol*. 948, A53, doi:10.1017/jfm.2022.736

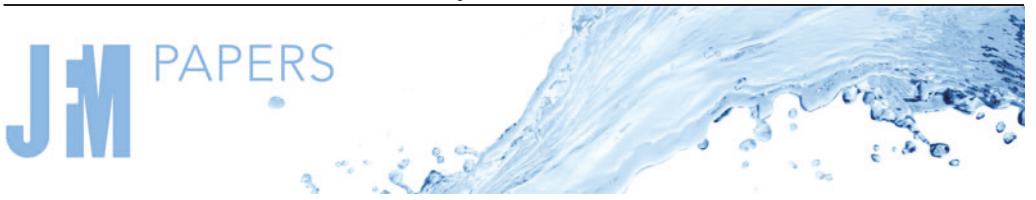

Oblique drop impact: can one infer the angle of impact?

Vanessa R. Kern[1],†, **Cathy Jin**[1], **J. B. Bostwick**[2] **and P. H. Steen**[1]

[1]Robert Frederick Smith School of Chemical and Biomolecular Engineering, Cornell University, Ithaca, NY 14850, USA

[2]Department of Mechanical Engineering, Clemson University, Clemson, SC 29634, USA

(Received 9 March 2022; revised 10 August 2022; accepted 22 August 2022)

During solid surface impact, a falling drop's energy is transformed into oscillations of its liquid/gas interface. We consider drop deposition during oblique impact in the capillary-ballistic regime characterized by high Reynolds number and moderate Weber number. We treat this as an inverse problem showing that post-impact observations of the frequency spectrum and modal partition of energy allow one to determine a drop's pre-impact characteristics and wetting properties. Our analysis is useful for quantifying contact-line dissipation during inertial spreading and can be used as a diagnostic technique for determining substrate wetting properties.

Key words: drops, contact lines, wetting and wicking

1. Introduction

Mathematician Marc Kac famously asked the question 'Can one hear the shape of a drum head?' in what is now synonymous with inverse problems in mathematical physics (Kac 1966). The conjecture is that if one knows the frequency spectrum of the wave equation for the drum head, then the shape (or part of the shape) can be inferred from the spectral data. Our study of oblique drop impact is conveniently framed as an analogy to this question. In the spirit of Kac, we ask a similar question: can one infer the angle of an impacting drop? More precisely, if we are given the Fourier spectra of the liquid/gas interface vibrations for an impacting drop, can we back out information such as its incident angle β, volume V and contact angle α_p?

The study of drop impact dates back to Worthington (1877, 1895), who first observed the forms generated by a drop of milk falling onto a glass plate, piquing a curiosity into drop impact lasting more than a century (Rein 1993; Rioboo, Tropea & Marengo 2001;

† Email address for correspondence: vrk24@cornell.edu

Richard, Clanet & Quéré 2002; Thoroddsen *et al.* 2005; Yeong *et al.* 2014; Aboud & Kietzig 2018). Edgerton & Killian (1954) were so moved by Worthington's corona splash that they developed the technology to capture a full-colour image that is now labelled as one of *TIME* magazine's most influential images of all time. Since the seminal work of Worthington, there has been sustained scientific interest in the complexity of drop impact as a canonical multiphysics and multiscale problem in fluid dynamics, whose understanding is subliminal yet necessary for the efficacy of crop sprays (Bergeron 2003; Mercer, Sweatman & Forster 2010; Delele *et al.* 2016; Massinon *et al.* 2017), aerosol drug delivery (Dolovich & Dhand 2011), quality control in rapid prototyping (Nayak *et al.* 2019; van der Meulen *et al.* 2020), and the mitigation of soil erosion from rain (Al-Durrah & Bradford 1982), and whose study has undergone a renaissance in the past few decades due to advances in high-speed imaging technologies (Versluis 2013).

Most prior studies of drop impact focus on normal impact with a solid substrate, de-emphasizing the role of liquid inertia and impact geometry (Yarin 2006; Grishaev *et al.* 2015; Josserand & Thoroddsen 2016). Here, we consider oblique drop impact onto partially wetting solids in the capillary-ballistic regime, defined by a moderate Reynolds number $Re \sim O(100)$, and a low Weber number $We \sim O(1)$. We treat the impacting event as an inverse problem, reconstructing the impact conditions from the post-impact liquid/gas vibration frequency spectrum and modal energy partitioning.

Kern, Bostwick & Steen (2021) have shown recently that for normal drop impact, the drop's liquid/gas interface vibrates in mode shapes predicted for sessile drops (Bostwick & Steen 2014; Chang *et al.* 2015; Steen, Chang & Bostwick 2019). In this paper, we show that the same is true for oblique drop impact. For reference, we summarize those results as they form the basis for our reconstruction of the liquid/gas interface shape. Bostwick & Steen (2014) showed that the interface deformation y for a sessile drop with pinned contact line obeys an operator equation

$$K[y] + \lambda^2 M[y] = 0, \tag{1.1}$$

where the M and K operators are related to the fluid inertia and restoring forcing of surface tension, respectively. A spectral method is used to reduce the operator equation to a standard eigenvalue problem using the Rayleigh–Ritz method. Equation (1.1) admits eigenvalue $\lambda_{[k,l]}$ and eigenmode $y_{[k,l]}$ solutions, defined by the mode number pair $[k, l]$ inherited from a spherical harmonic classification scheme with $k + l =$ even, needed to enforce the no-penetration condition on the solid support. Here, k represents the number of nodes that a shape traces with its base state in side view, and l represents the number of sectors or lines of symmetry that a shape has when viewed from above. Typical mode shapes are shown in figure 1. Each resonance mode has a natural frequency $f_{[k,l]}$ determined by the drop's pinned contact angle α_p (which can fall anywhere in the range of the contact angle hysteresis), contact-line radius a (equivalently, volume V), surface tension σ, and density ρ. The predicted mode shapes form an orthogonal basis, and we use this fact to resolve the shape-change dynamics of the vibrating interface for a post-impact drop.

2. Experiment

Drops are formed by pumping de-ionized (DI) water at 1 µl s^{-1} from a ramé-hart auto-dispensing system through 22 or 30 gauge syringe tips, resulting in drops of 13.8 ± 0.1 µl or 6.3 ± 0.1 µl, respectively. The formed drops are allowed to break freely from the syringe tip and accelerate due to gravity from a height h ranging from 2.8 mm to

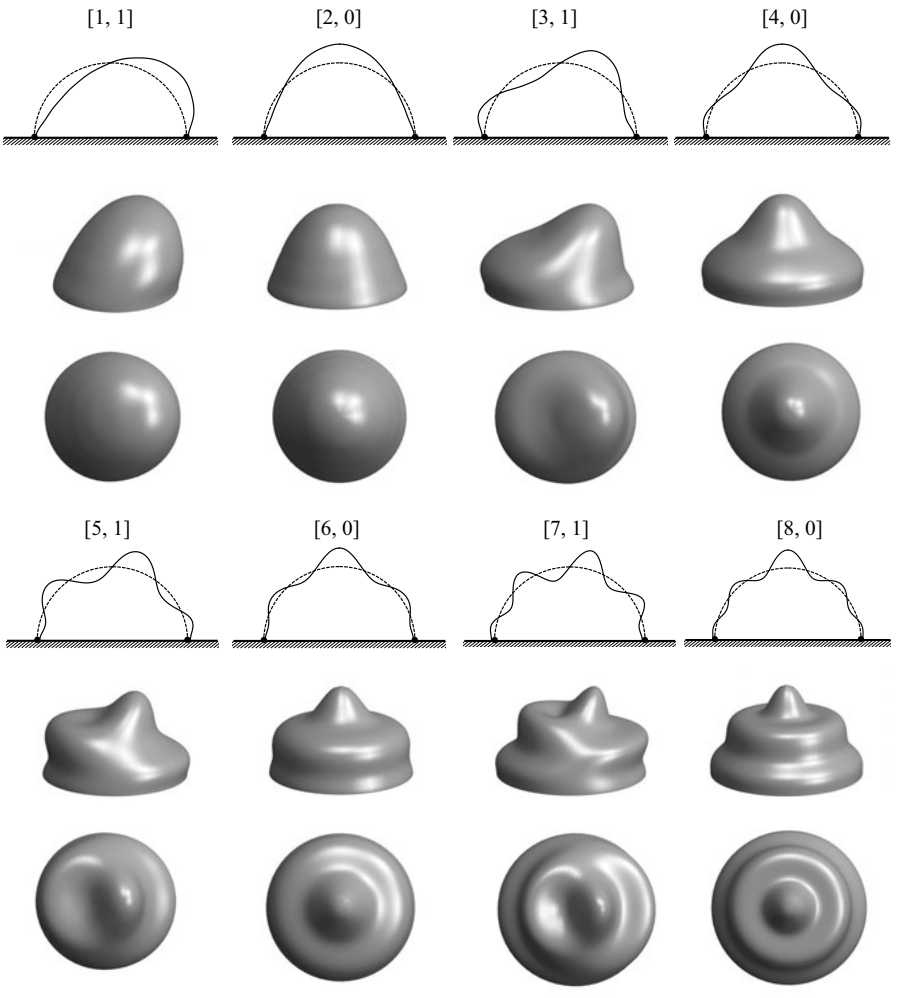

Figure 1. Sessile drop mode shapes defined by mode number pair $[k, l]$ in two-dimensional polar, three-dimensional side, and three-dimensional top views. Here, $\alpha = 90^\circ$.

25.1 mm above a substrate inclined at angle $\beta = 0$–60° from the horizontal, as shown in figure 2(a). This corresponds to impact Weber numbers $We \equiv 2\rho g h d/\sigma = 0$–16, where d is the pre-impact drop diameter. Drop radii are smaller than the capillary length scale $\ell_c = \sqrt{\sigma/\rho g}$, thus gravity can be ignored. The substrates are modified chemically to produce different contact angles $\bar{\alpha}$ and hysteresis $\Delta\alpha$, as shown in table 1. Details about the surface preparation can be found in Appendix A.

The impacting event is recorded using a Redlake Motion Xtra HG-XL high-speed camera at a minimum frame rate of 5000 fps. The motion of the drop's interface was post-processed in MATLAB by tracking the liquid/gas interface along a ray extending from the drop's centre using subpixel edge detection techniques (Trujillo-Pino *et al.* 2013; Trujillo-Pino 2019). Fast Fourier transforms (FFTs) were performed to determine the drop's frequency spectrum.

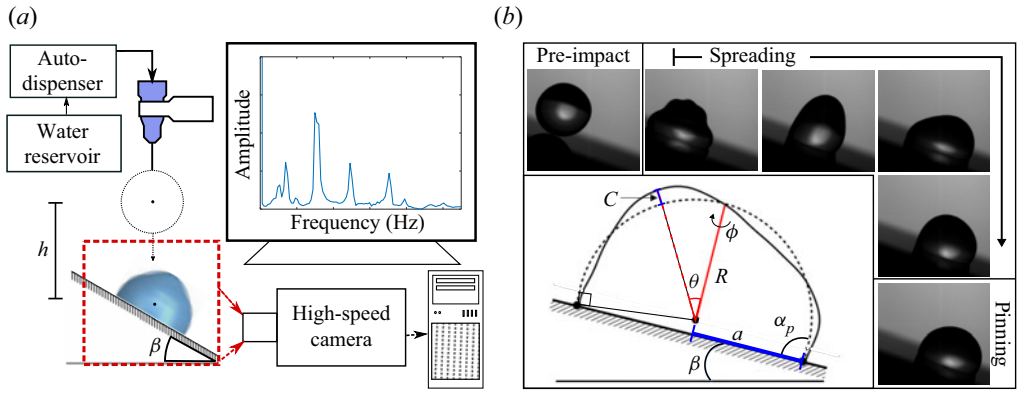

Figure 2. Experimental set-up. (*a*) Water drops are generated from an auto-dispenser and impact a substrate inclined at angle β. High-speed imagery captures the impacting event. (*b*) Post-impact, the contact line spreads before coming to rest at pinning angle α_p. Post-pinning, the drop's motion is restricted to liquid/gas interfacial oscillations according to sessile drop theory (Bostwick & Steen 2014). The sessile drop geometry is defined by the spherical cap's radius R, the deformation of the liquid/gas interface normal to the base state c, the drop's footprint radius a, and the polar and azimuthal angles θ, ϕ, respectively.

Code	Substrate	Modification	$\bar{\alpha}$ (deg.)	$\Delta\alpha_a$ (deg.)
A	Glass	3-Aminopropyl triethoxysilane (APTES)	68.8	21.9
F	Glass	Heptadecafluoro-1,1,2,2- tetrahydrododecyl trichlorosilane	98.6	14.7
P	Silicon	Trimethylsiloxy terminated poly(dimethylsiloxane) (PDMS)	105.5	7.8

Table 1. Substrate identification with wetting properties defined by the equilibrium angle $\bar{\alpha}$ and contact-angle hysteresis $\Delta\alpha$.

3. Results

The impacting event can be decomposed into three stages as shown in figure 2(*b*): 'pre-impact', 'spreading' (post-impact) and 'pinning' (post-impact). Pre-impact is defined by the drop falling freely until coalescence with the substrate. Spreading is defined by advancing and receding inertial motion of the contact line, separating the liquid/solid/gas phases. Pinning is defined as the instant in time when the contact line comes to its final resting position, after which the liquid/gas interface oscillates, dissipating energy through viscous dissipation. This final resting position can be characterized by the drop's pinning contact angle α_p, which can fall anywhere within the the drop's contact angle hysteresis, as illustrated in figure 4(*a*) by each substrate's range of α_p. We consider only deposition drop impacts, where no splashing, receding breakup or rebound occurs, as illustrated in figure 2(*b*), and focus on liquid/gas vibrations during pinning.

The liquid/gas interface oscillates in a linear combination of mode shapes, $y = \sum c_{[k,l]}\, y_{[k,l]}$, described by theory (Bostwick & Steen 2014, 2016). Each mode $y_{[k,l]}$ has a unique polar angle θ maximizing that mode's contribution to the interface shape $c_{[k,l]}$ defined as the disturbance normal to the drop's base state as measured at the onset of pinning (see Appendix B).

During normal drop impact, $\beta = 0°$, we have shown that during pinning, the drop vibrates in a linear combination of axisymmetric $l = 0$ modes with corresponding frequencies $f_{[k,0]}$ (Kern *et al.* 2021). Figure 3(*a*) shows that for oblique impact, the

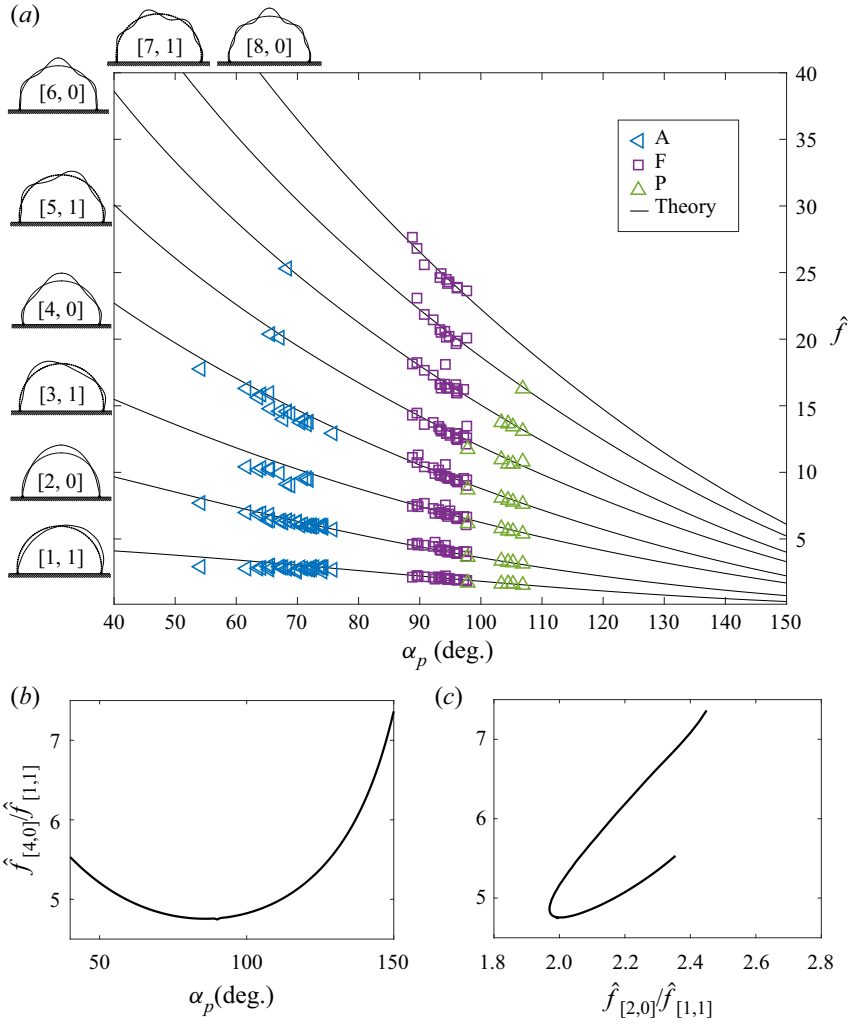

Figure 3. Scaled frequency ratios determine α_p. (*a*) Experimental and theoretical scaled frequencies $\hat{f}$ against pinning angle α_p for the $l = 0, 1$ mode shapes. Measured $\hat{f}$ are independent of β. (*b*) The frequency ratio $\hat{f}_{[4,0]}/\hat{f}_{[1,1]}$ is not monotonic with respect to α_p, therefore a single frequency ratio $\hat{f}_{[k,l]}/\hat{f}_{[1,1]}$ is not enough information to determine α_p. (*c*) By knowing two frequency ratios $\hat{f}_{[k,l]}/\hat{f}_{[1,1]}$, α_p can be determined uniquely (α_p increases in the clockwise direction).

frequency spectrum consists of both the $l = 0$ and $l = 1$ modes. The frequencies $\hat{f}$ were measured by performing an FFT of the time trace of c at a polar angle θ that maximizes $c_{[k,l]}$ for each mode shape. Here, $\hat{f}$ is scaled by the capillary time τ:

$$\hat{f} = f\tau = f\sqrt{\frac{\rho a^3}{\sigma}}, \tag{3.1}$$

where a is the footprint radius of the drop. For $l = 0$ modes, $c_{[k,0]}$ is maximized at the drop's apex, $\theta = 0^\circ$, but for the $l = 1$ modes, the θ that maximizes $c_{[k,1]}$ depends on the pinning angle α_p. We note from figure 3(*a*) that $\hat{f}$ is independent of β and that experiments

follow theoretical predictions well over a range of pinning angles α_p. We also note a monotonic relationship in the frequency spacing between modes.

To infer the pinning angle α_p from the spacing in the frequency spectrum between any two modes is not sufficient, as α_p is double-valued with respect to $\hat{f}_{[k,0]}/\hat{f}_{[1,1]}$ (cf. Figure 3*b*). However, knowing two frequency spacings is sufficient. As such, a plot of $\hat{f}_{[k_1,0]}/\hat{f}_{[1,1]}$ against $\hat{f}_{[k_2,0]}/\hat{f}_{[1,1]}$, where $k_1 \neq k_2$, provides a unique determination of α_p (cf. figure 3*c*), with α_p increasing as the curve is traversed in a clockwise direction. This invariance of $\hat{f}$ with β combined with the monotonic relationship between $\hat{f}$ and α_p implies that we can determine the pinning angle α_p from knowledge of the resonance frequency of any two modes $\hat{f}_{[k,l]} \neq \hat{f}_{[1,1]}$ scaled by $\hat{f}_{[1,1]}$, such that $\hat{f}_{[k_1,l_1]}/\hat{f}_{[1,1]} = f_{[k_1,l_1]}/f_{[1,1]}$ and $\hat{f}_{[k_2,l_2]}/\hat{f}_{[1,1]} = f_{[k_2,l_2]}/f_{[1,1]}$. Once the pinning angle α_p is known, the radius R can be determined from theory, given the liquid properties σ, ρ, resonance frequency of any mode $f_{[k,l]}$, and pinning angle α_p.

3.1. *Role of inclination angle β*

The decomposition of the liquid/gas interface oscillations into modal components shows that $c_{[k,l]}$ is maximized for each $l = 0$, 1 mode at a specific polar angle θ. Figures 4(*a*)–4(*c*) show a set of FFTs performed for a single experiment at different θ. For all $l = 0$ modes, $c_{[k,0]}$ is maximized at the drop's apex $\theta = 0^\circ$ (cf. figure 4*a*), whereas for the $l = 1$ modes, $c_{[k,1]}$ is maximized at $\theta \neq 0^\circ$ (cf. figures 4*b*,*c*). These values of θ can be found from theory by knowing the drop's liquid properties (σ, ρ) and α_p (Bostwick & Steen 2014). Note that figures 4(*a*)–4(*c*) show that changing θ does not shift $f_{[k,l]}$, but only the ratios of $\bar{c}_{[k,l]}$ for each mode, where $\bar{c}_{[k,l]}$ denotes the average magnitude of c measured throughout pinning. Similarly, each mode shape has a set of θ where $c = 0$, corresponding to nodes. For example, each mode with $l > 0$ has a node at its apex $\theta = 0^\circ$, as can be seen for the [3, 1] mode in figure 2(*b*). For each θ corresponding to a node, the corresponding frequency $\hat{f}$ is muted in the FFT, as shown in figures 4(*a*)–4(*c*).

The decomposition of the frequency spectrum in figure 4 into $l = 0$, 1 components can yield information about the inclination angle β. To illustrate, let us motivate by considering the case of an elastic collision between a point mass and substrate. The principle of momentum conservation dictates that a ball bouncing off a substrate will have an incident angle equal to its deflection angle. This idea suggests that we consider the drop as a point mass and focus on the motion of the drop's centre of mass (CoM) during pinning. Figure 5(*a*) shows the motion of a drop's CoM for a sessile drop with typical $l = 0$ and $l = 1$ mode shapes (Wesson & Steen 2020). The $l = 0$ modes have CoM motion that is solely normal to the substrate ($\hat{z}$ direction), whereas $l = 1$ mode shapes have CoM motion in both the $\hat{z}$ and $\hat{x}$ directions, with the [1, 1] mode being nearly horizontal ($\hat{x}$ direction). The primary carriers of the normal and horizontal CoM motions are the [2, 0] and [1, 1] modes, respectively.

During normal $\beta = 0^\circ$ impact, only $l = 0$ modes are excited, and the CoM motion is purely in the $\hat{z}$ direction (Kern *et al.* 2021). For drop impacts with $\beta \neq 0^\circ$, both $l = 0$ (pure $\hat{z}$ motion) and $l = 1$ ($\hat{z}$ and $\hat{x}$ motion) modes are excited, as shown in figure 3(*a*). As β increases, we expect more of the drop's CoM motion to partition into $\hat{x}$ motion ($l = 1$ modes), as could be inferred from figure 5(*a*). Figures 5(*b*) and 5(*c*) plot the modal decomposition $c_{[k,l]}/R$ for a range of drop impacts over increasing β with α_p held constant. We see results that meet our expectations. For $l = 0$ modes ([2, 0] shown), we see a decrease in $c_{[2,0]}$ as β increases, whereas for the [1, 1] mode, we see an increase in

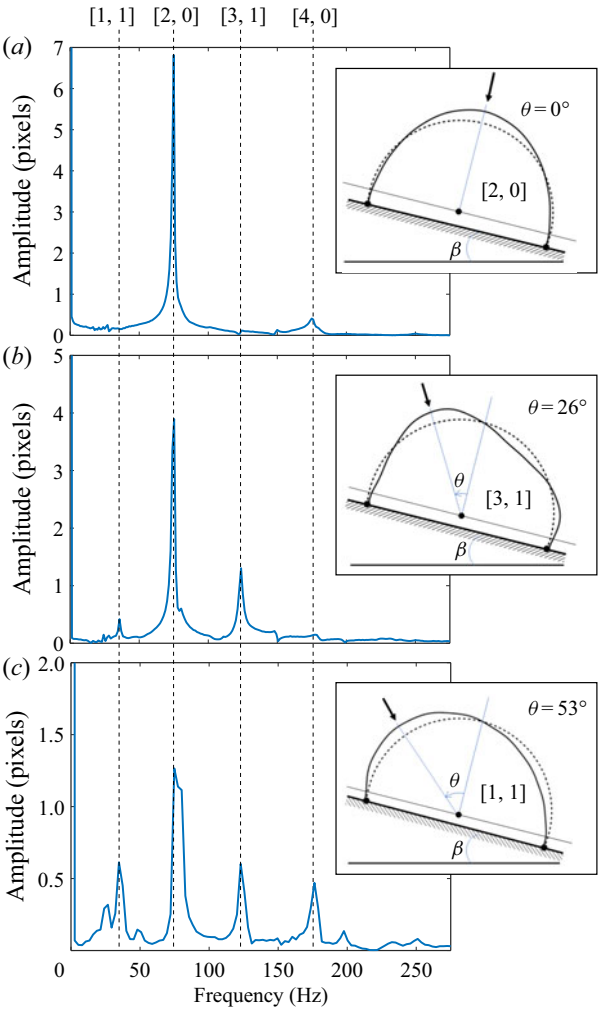

Figure 4. Fast Fourier transforms of the drop's liquid/gas interface measured at different interface locations θ for a single experiment. Here, $R = 1.76$ mm, $\alpha_p = 97.7^\circ$ and $\beta = 18^\circ$. Note the different y-axis scales and how the positions of the frequency peaks do not shift when the measurement angle θ is varied. Interface disturbances $c_{[k,l]}$ are maximized at (*a*) $\theta = 0^\circ$ for the [2, 0] mode, (*b*) $\theta = 26^\circ$ for the [3, 1] mode, and (*c*) $\theta = 53^\circ$ for the [1, 1] mode.

$c_{[1,1]}$ as β increases. Note the monotonic relationship between $\beta \in [0^\circ, 60^\circ]$ and $c_{[k,l]}/R$ shown in figures 5(*b*) and 5(*c*). The ratio $c_{[2,0]}/c_{[1,1]}$ is both resolvable and monotonic for $\beta \in [0^\circ, 30^\circ]$, as shown in figure 5(*d*), implying that knowledge of β for an individual impact could then be inferred. That is, we could predict the inclination angle β from the spectral data for $c_{[2,0]}$ and $c_{[1,1]}$, assuming that the characteristic $c_{[2,0]}/c_{[1,1]}$ against β relation was previously determined for the system.

4. Concluding remarks

In this work, we performed experiments of oblique drop impact on partially-wetting substrates and asked the question 'Can one infer the angle of impact?' from the spectral data, thus making an analogy with the famous inverse problem of Kac (1966): 'Can one

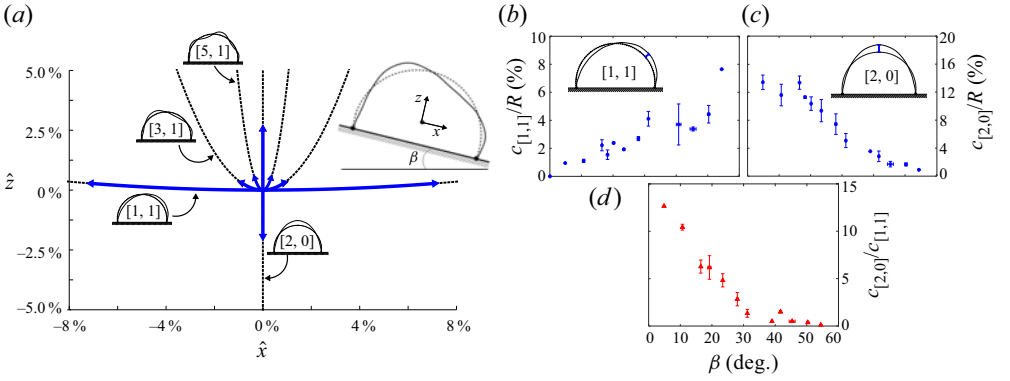

Figure 5. Centre of mass trajectories explain liquid/gas interface disturbance decomposition. (*a*) Centre of mass (CoM) motion trajectories. Dotted lines represent extended trajectories (Wesson & Steen 2020). Solid blue lines represent CoM trajectories corresponding to 10 % disturbances of the interface, $c/R = 0.1$. The CoM of the $l = 0$ modes moves exclusively in the $\hat{z}$ direction, while the [1, 1] mode is primarily in the $\hat{x}$ direction. The CoM motions of the [3, 1], [5, 1], [1, 1] modes have components in both the $\hat{x}$ and $\hat{z}$ directions. (*b–d*) Decomposition of liquid/gas interface disturbance $c_{[k,l]}$ against impact angle β for two sets of experiments. Impact kinetic energy ranged from 15 % to 25 % of the pre-impact liquid/gas surface energy. As β increases: (*b*) $c_{[1,1]}$ increases and (*c*) $c_{[2,0]}$ decreases, monotonically. Note the different *y*-axis scales. (*d*) The ratio $c_{[2,0]}/c_{[1,1]}$ decreases monotonically with β, allowing one to determine β uniquely from the modal decomposition.

hear the shape of a drum?' Not all inverse problems are solvable. Even for Kac's drum, a solution starting from only the frequency spectrum is impossible (Gordon & Webb 1996). However, aspects of the solution, such as the area of the drum's interface Ω, can still be known. Here, we found that knowledge of the drop's post-impact frequency spectrum $\hat{f}$ and liquid properties (σ, ρ) allows us to determine uniquely the drop's rest angle α_p and radius R (equivalently, volume V), analogous to Kac's drum area Ω. With regard to the latter, we could have inferred the surface tension σ just as easily given a known drop volume V of density ρ, and this may be an important measurement for freshly deposited drops. Next, we showed how to determine the inclination angle β from the modal decomposition of the liquid/gas vibrations $c_{[2,0]}/c_{[1,1]}$. Which leaves open the question, can the relation between $c_{[2,0]}/c_{[1,1]}$ and β be determined *a priori*?

Our results have broad underlying implications for real-time monitoring of manufacturing processes utilizing drop deposition, e.g. the fabrication of solar cells (Stüwe *et al.* 2015; Karunakaran *et al.* 2019), LEDs (Haverinen, Myllyla & Jabbour 2010) and electroluminescent displays (Kim *et al.* 2015), as well as the analysis of blood spatter patterns in forensic science (Raymond, Smith & Liesegang 1996; Hulse-Smith & Illes 2007; Comiskey *et al.* 2016). By analysing the impacting event from an energy perspective, contact-line dissipation during spreading can be calculated via the difference between the pre-impact energy and the pinning energy stored in the liquid/gas oscillations (Kern *et al.* 2021). This spreading energy is related directly to the contact-line dynamics and the contact-angle hysteresis of the liquid/gas/solid system. Our work in this capillary-ballistic spreading regime is particularly noteworthy and contrasts the vast majority of studies focusing on viscous-dominated spreading that gives rise to the well-known Tanner's law (Grishaev *et al.* 2015), all while considering the complex liquid/gas dynamics post oblique impact.

Acknowledgements. We acknowledge Professor P.H. Steen's role in leading this research, and note his passing before the time of publishing. We are honoured to be able to continue this work and bring it to the field.

We would also like to acknowledge the insight provided by Y. Xia, E. Wesson, J. McCraney, S. Weinstein, J. Ludwicki, J. Mattson and S. Daniel throughout completion of this work.

Funding. The authors gratefully acknowledge support from NSF grants 1530522, 1637960 and 1935590.

Declaration of interests. The authors report no conflict of interest.

Author ORCIDs.
Vanessa R. Kern https://orcid.org/0000-0002-9799-2733;
J. B. Bostwick https://orcid.org/0000-0001-7573-2108;
P. H. Steen https://orcid.org/0000-0002-0507-9438.

Appendix A. Materials

Glass slides (VWR VistaVision, catalog no. 16004-430, 3 in × 1 in × 1 mm), sulphuric acid (95–98 % min., MW 98.08, CAS# 7664-93-9), ethanol (reagent alcohol, absolute, CAS# 64-17-5; Macron Chemicals), toluene (99.5 % min., MW 92.14, CAS# 108-88-3), and acetone (CAS# 67-64-1; Macron Chemicals) were purchased from VWR International (Radnor, PA, USA). Silicon wafers (Silicon Quest International, catalogue no. 808-007) were purchased from Silicon Quest International (San Jose, CA, USA). Hydrogen peroxide (50 wt%, SKU 516813-500ML, CAS# 7722-84-1, MW 34.01 g mol^{-1}) was purchased from Sigma-Aldrich (St Louis, MO, USA). Fluorosilane (heptadecafluoro-1,1,2,2-tetrahydrododecyl trichlorosilane, CAS# 78560-44-8, MW 581.56), trimethylsiloxy terminated poly(dimethylsiloxane) (PDMS) (Gelest, Product Code DMS-T22) and APTES 99+% were purchased from Gelest (Morrisville, PA, USA). Light mineral oil (CAS# 8042-47-5) was purchased from Fisher Scientific (Pittsburgh, PA, USA). Liquid nitrogen and high-purity compressed nitrogen were purchased from Airgas (Radnor, PA, USA). A 14–30 g assortment of syringe tips (Part no. 922-005) were purchased from CML supply (via Amazon).

A.1. *Fluorosilane substrate preparation*

Glass slides were sonicated (Ultrasonic Cleaner, model B2500A-DTH, VWR) for 20 min in water to remove solid particles from their surfaces, then immersed in piranha solution (70 % sulphuric acid/30 % hydrogen peroxide) for 20 min to remove any organic contaminants. The slides were then rinsed with DI water (purified by an Elga Ultra SC MK2, Siemens) and kept immersed until needed. Two grams of mineral oil and 2 µl fluorosilane were deposited in a plastic Petri dish and homogenized via manually stirring. The fluorosilane/mineral oil solution was placed in a vacuum desiccator. A trap in the line between the desiccator and vacuum pump was filled with liquid nitrogen to prevent pump corrosion from vaporized fluorosilane. A vacuum was pulled on the desiccator for 30 min to remove any gaseous impurities in the fluorosilane/mineral oil solution. The glass slides were removed from the DI water, blown dry with high-purity compressed nitrogen, and placed onto a clean dry rack. The vacuum on the desiccator was slowly broken, and the rack holding the glass slides was placed into the desiccator alongside the fluorosilane/mineral oil solution. A vacuum was pulled on the desiccator, now containing both the fluorosilane/mineral oil solution and the rack holding the glass slides, for 30 min. The desiccator was sealed and allowed to set for a minimum of 3 h to allow the deposition to react. Prior to experimental use, the slides were rinsed with (1) ethanol, (2) DI water, and dried with high-purity nitrogen gas.

A.2. *APTES substrate preparation*

Glass slides were sonicated (Ultrasonic Cleaner, model B2500A-DTH, VWR) for 20 min in water to remove solid particles from their surfaces, and then immersed in piranha solution (70 % sulphuric acid/30 % hydrogen peroxide) for 20 min to remove any organic contaminants. The slides were then rinsed with DI water (purified by an Elga Ultra SC MK2, Siemens) and kept immersed until needed. The interior of a 400 ml staining dish and glass rack were rinsed with (1) soap, (2) reverse osmosis water, (3) ethanol and (4) acetone, blown dry with compressed nitrogen, and baked dry in the oven for 15 min. 200 ml acetone, 8 ml APTES and the glass rack were deposited in the cleaned staining dish. Each glass slide was blown dry with high-purity compressed nitrogen and set in the APTES/acetone solution on the glass rack. The slides were soaked for 20 min. After soaking, the slides were heated in the oven at 85 °C for 20 min. Prior to experimental use, the slides were rinsed with (1) ethanol, (2) DI water, and dried with high-purity nitrogen gas.

A.3. *PDMS substrate preparation*

Silicon wafers were cut into 1 cm $\times$ 1 cm pieces and then immersed in piranha solution (70 % sulphuric acid/30 % hydrogen peroxide) for 20 min to remove any organic contaminants. The slides were then plasma cleaned (Harrick Plasma BASIC) at 18 W and 300 mmTorr for 30 min. The slides were then placed inside 20 ml borosilicate glass scintillation vials and wetted with DMS-T22 as received. The vials were then capped and baked in an oven at 100 °C for 24 h. Prior to experimental use, the surfaces were rinsed with (1) toluene, (2) acetone and (3) DI water.

Appendix B. Calculating c

MATLAB code was written to track the liquid/gas interface along a ray extending from the drop's centre using subpixel edge-detection techniques. A fast Fourier transform (FFT) of this resultant time trace was calculated over the entirety of pinning. The initial perturbation of the liquid/gas interface corresponding to each mode, $c_{[k,0]}$, was calculated from the FFT, and the decay rate of the corresponding mode ($\gamma_{[k,0]}$) was shown to be constant throughout pinning. The $\gamma_{[k,0]}$ were measured by breaking the time sequence of images into segments obeying the Nyquist condition – which states that a signal must be sampled at a rate of at least twice the highest frequency component to be observed – performing a FFT on each segment, and measuring the amplitude of each frequency peak as it decayed.

References

Aboud, D.G.K. & Kietzig, A.-M. 2018 On the oblique impact dynamics of drops on superhydrophobic surfaces. Part II: Restitution coefficient and contact time. *Langmuir* **34** (34), 9889–9896.

Al-Durrah, M.M. & Bradford, J.M. 1982 Parameters for describing soil detachment due to single waterdrop impact. *Soil Sci. Soc. Am. J.* **46** (4), 836–840.

Bergeron, V. 2003 Designing intelligent fluids for controlling spray applications. *C.R. Phys.* **4** (2), 211–219.

Bostwick, J.B. & Steen, P.H. 2014 Dynamics of sessile drops. Part 1. Inviscid theory. *J. Fluid Mech.* **760**, 5–38.

Bostwick, J.B. & Steen, P.H. 2016 Response of driven sessile drops with contact-line dissipation. *Soft Matt.* **12** (43), 8919–8926.

Chang, C.-T., Bostwick, J.B., Daniel, S. & Steen, P.H. 2015 Dynamics of sessile drops. Part 2. Experiment. *J. Fluid Mech.* **768**, 442–467.

COMISKEY, P.M., YARIN, A.L., KIM, S. & ATTINGER, D. 2016 Prediction of blood back spatter from a gunshot in bloodstain pattern analysis. *Phys. Rev. Fluids* **1** (4), 043201.

DELELE, M.A., NUYTTENS, D., DUGA, A.T., AMBAW, A., LEBEAU, F., NICOLAI, B.M. & VERBOVEN, P. 2016 Predicting the dynamic impact behaviour of spray droplets on flat plant surfaces. *Soft Matt.* **12** (34), 7195–7211.

DOLOVICH, M.B. & DHAND, R. 2011 Aerosol drug delivery: developments in device design and clinical use. *Lancet* **377** (9770), 1032–1045.

EDGERTON, H.E. & KILLIAN, J.R. 1954 *Flash! Seeing the Unseen by Ultra High-Speed Photography*. CT Branford Company.

GORDON, C. & WEBB, D. 1996 You can't hear the shape of a drum. *Am. Sci.* **84** (1), 46–55.

GRISHAEV, V., IORIO, C.S., DUBOIS, F. & AMIRFAZLI, A. 2015 Complex drop impact morphology. *Langmuir* **31** (36), 9833–9844.

HAVERINEN, H.M., MYLLYLA, R.A. & JABBOUR, G.E. 2010 Inkjet printed RGB quantum dot-hybrid LED. *J. Display Technol.* **6** (3), 87–89.

HULSE-SMITH, L. & ILLES, M. 2007 A blind trial evaluation of a crime scene methodology for deducing impact velocity and droplet size from circular bloodstains. *J. Forensic Sci.* **52** (1), 65–69.

JOSSERAND, C. & THORODDSEN, S.T. 2016 Drop impact on a solid surface. *Annu. Rev. Fluid Mech.* **48**, 365–391.

KAC, M. 1966 Can one hear the shape of a drum? *Am. Math. Mon.* **73** (4P2), 1–23.

KARUNAKARAN, S.K., ARUMUGAM, G.M., YANG, W., GE, S., KHAN, S.N., LIN, X. & YANG, G. 2019 Recent progress in inkjet-printed solar cells. *J. Mater. Chem.* A **7** (23), 13873–13902.

KERN, V.R., BOSTWICK, J.B. & STEEN, P.H. 2021 Drop impact on solids: contact-angle hysteresis filters impact energy into modal vibrations. *J. Fluid Mech.* **923**, A5.

KIM, B.H., *et al.* 2015 High-resolution patterns of quantum dots formed by electrohydrodynamic jet printing for light-emitting diodes. *Nano Lett.* **15** (2), 969–973.

MASSINON, M., DE COCK, N., FORSTER, W.A., NAIRN, J.J., MCCUE, S.W., ZABKIEWICZ, J.A. & LEBEAU, F. 2017 Spray droplet impaction outcomes for different plant species and spray formulations. *Crop Prot.* **99**, 65–75.

MERCER, G.N., SWEATMAN, W.L. & FORSTER, W.A. 2010 A model for spray droplet adhesion, bounce or shatter at a crop leaf surface. In *Progress in Industrial Mathematics at ECMI 2008*, pp. 945–951. Springer.

VAN DER MEULEN, M.-J., REINTEN, H., WIJSHOFF, H., VERSLUIS, M., LOHSE, D. & STEEN, P. 2020 Nonaxisymmetric effects in drop-on-demand piezoacoustic inkjet printing. *Phys. Rev. Appl.* **13** (5), 054071.

NAYAK, L., MOHANTY, S., NAYAK, S.K. & RAMADOSS, A. 2019 A review on inkjet printing of nanoparticle inks for flexible electronics. *J. Mater. Chem.* C **7** (29), 8771–8795.

RAYMOND, M.A., SMITH, E.R. & LIESEGANG, J. 1996 The physical properties of blood – forensic considerations. *Sci. Justice: J. Forensic Sci. Soc.* **36** (3), 153–160.

REIN, M. 1993 Phenomena of liquid drop impact on solid and liquid surfaces. *Fluid Dyn. Res.* **12** (2), 61–93.

RICHARD, D., CLANET, C. & QUÉRÉ, D. 2002 Contact time of a bouncing drop. *Nature* **417** (6891), 811–811.

RIOBOO, R., TROPEA, C. & MARENGO, M. 2001 Outcomes from a drop impact on solid surfaces. *Atomiz. Sprays* **11** (2), 155–165.

STEEN, P.H., CHANG, C.-T. & BOSTWICK, J.B. 2019 Droplet motions fill a periodic table. *Proc. Natl Acad. Sci.* **116** (11), 4849–4854.

STÜWE, D., MAGER, D., BIRO, D. & KORVINK, J.G. 2015 Solvent inkjet printing process for the fabrication of polymer solar cells. *Adv. Mater.* **27**, 599–626.

THORODDSEN, S.T., ETOH, T.G., TAKEHARA, K., OOTSUKA, N. & HATSUKI, Y. 2005 The air bubble entrapped under a drop impacting on a solid surface. *J. Fluid Mech.* **545**, 203–212.

TRUJILLO-PINO, A. 2019 Accurate subpixel edge location. MATLAB Central File Exchange. Available at: https://www.mathworks.com/matlabcentral/fileexchange/48908-accurate-subpixel-edge-location.

TRUJILLO-PINO, A., KRISSIAN, K., ALEMÁN-FLORES, M. & SANTANA-CEDRÉS, D. 2013 Accurate subpixel edge location based on partial area effect. *Image Vis. Comput.* **31** (1), 72–90.

VERSLUIS, M. 2013 High-speed imaging in fluids. *Exp. Fluids* **54** (2), 1458.

WESSON, E. & STEEN, P. 2020 Steiner triangular drop dynamics. *Chaos* **30** (2), 023118.

WORTHINGTON, A.M. 1877 XXVIII. On the forms assumed by drops of liquids falling vertically on a horizontal plate. *Proc. R. Soc. Lond.* **25** (171–178), 261–272.

WORTHINGTON, A.M. 1895 *The Splash of a Drop*. Society for Promoting Christian Knowledge.

YARIN, A.L. 2006 Drop impact dynamics: splashing, spreading, receding, bouncing. *Annu. Rev. Fluid Mech.* **38**, 159–192.

YEONG, Y.H., BURTON, J., LOTH, E. & BAYER, I.S. 2014 Drop impact and rebound dynamics on an inclined superhydrophobic surface. *Langmuir* **30** (40), 12027–12038.